Bulletin of the Seismological Society of America, Vol. 97, No. 3, pp. 881–900, June 2007, doi: 10.1785/0120060044

Ⓔ

Sensitivity of Ground-Motion Simulations to Earthquake Source Parameters: A Case Study for Istanbul, Turkey

by Mathilde B. Sørensen,* Nelson Pulido, and Kuvvet Atakan

Abstract Following the disastrous earthquakes in Izmit and Düzce along the North Anatolian fault in 1999, the earthquake hazard in the Istanbul area became a great concern. In this study we simulate strong ground motions caused by a scenario earthquake (*M* 7.5) in the Marmara Sea, and investigate the effect of varying the input parameters on the broadband frequency ground motion. Simulations are based on a multiasperity source model that involves the combined rupture of the North Anatolian fault segments beneath the Marmara Sea. We use a hybrid model combining a deterministic simulation of the low frequencies (0.1–1.0 Hz) with a semistochastic simulation of the high frequencies (1.0–10.0 Hz). Computation at each frequency range is performed separately and the total ground motion is combined in the time domain. Computations are linear and are performed at bedrock level, thereby not taking any effect of local geological conditions into account. We calculate a total of 17 earthquake scenarios corresponding to different source and attenuation parameters to study their effect on the ground motion. The most significant parameters in terms of ground-shaking level are the rise time, rupture velocity, rupture initiation point, and stress drop. The largest variability of strong ground motions is observed in regions adjacent to asperities and is associated with frequencies higher than 5 Hz. For lower frequencies our simulated velocity spectra within the Istanbul area are fairly stable among scenarios. The average standard deviations of all ground-motion measures are less than 35% of the mean.

Online material: Figures of peak ground acceleration and peak ground velocity and their differences to the reference scenario values.

Introduction

The city of Istanbul is under a significant seismic hazard because its proximity to the Marmara Sea segment of the North Anatolian fault (NAF) (Fig. 1a). During the past century there has been a westward migration of large, destructive earthquakes along the NAF with the latest events occurring in Izmit and Ducze in 1999 (e.g., Barka *et al.*, 2002). Since these large earthquakes, there has been an increase in the Coulomb stress along the Marmara Sea segment (Hubert-Ferrari *et al.*, 2000) which, together with the fact that no large earthquakes have occurred at least since 1766 (Barka *et al.*, 2002), indicates that a large earthquake is likely to break this part of the NAF within the lifetime of the present city environment (Parsons *et al.*, 2000; Parsons, 2004).

Seismic hazard in Istanbul has previously been estimated using probabilistic methods (Atakan *et al.*, 2002; Erdik *et al.*, 2004). For future risk mitigation and city planning, a detailed estimate of the seismic hazard in Istanbul is needed. Recently, increased knowledge of the NAF within the Marmara Sea allowed other methods to be applied. Pulido *et al.* (2004) modeled the bedrock ground motions due to a finite-extent scenario earthquake source (*M* 7.5) in the Marmara Sea using a hybrid broadband simulation technique, and hereby gave a first insight to the complexity of ground shaking to be expected in a future earthquake. Such results are important because of their direct engineering implications with critical information available about frequency content, absolute level, and duration of ground motion. However, the uncertainties related to defining the source parameters of a scenario earthquake influence the results in a way which until now has not been well resolved. Our main objective is therefore to study and quantify the effect of these uncertainties.

In the present study we simulate ground motions due to several earthquake scenarios in the Marmara Sea using the methodology of Pulido *et al.* (2004), and compare with a

*Present address: GeoForschungsZentrum Potsdam, Section 5.3, Telegrafenberg, 14473 Potsdam, Germany; sorensen@gfz-potsdam.de.

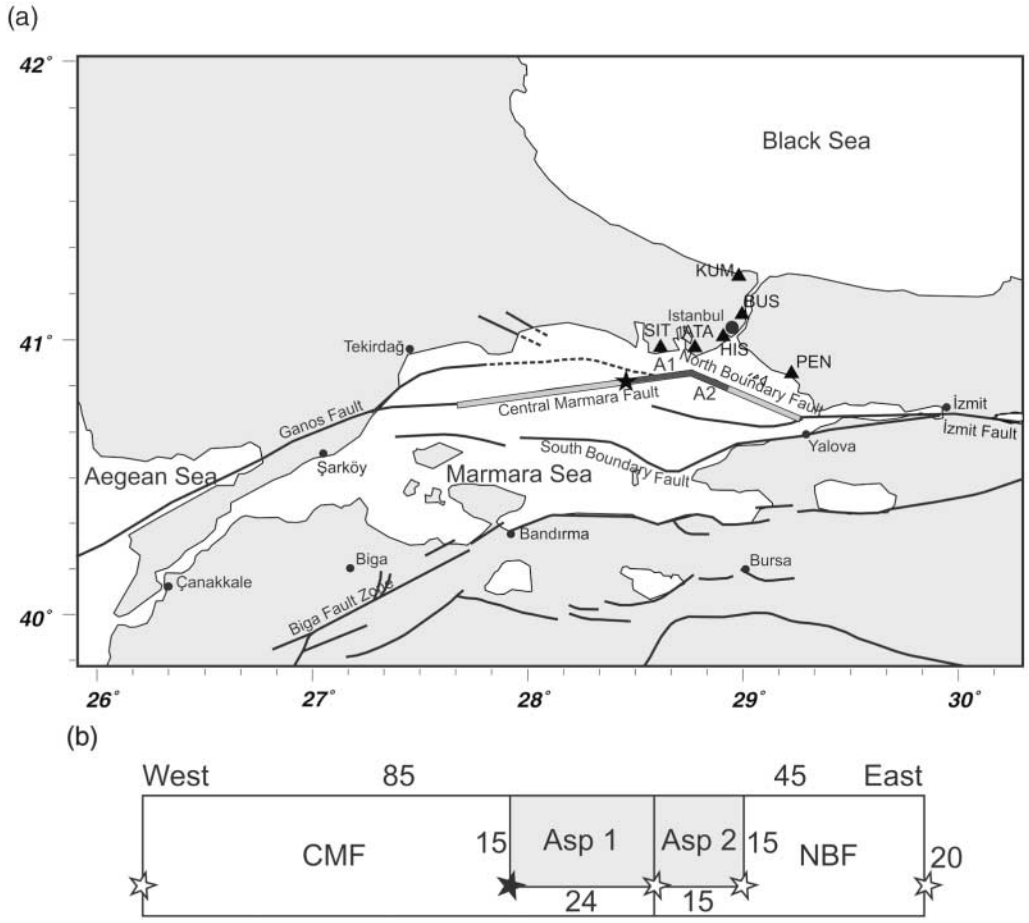

Figure 1. Geometry of the reference scenario. (a) Map of active faulting in the Marmara Sea region (redrawn from Okay *et al.*, 2000). The most significant faults in the region are shown as black lines. The rupturing fault segment is shown as a thick gray line; asperities are shown as darker-gray line segments. The star shows the rupture initiation point. A1 and A2 mark asperities 1 and 2, respectively. Filled triangles indicate the locations of the six sites analyzed in terms of spectral velocity and spectral acceleration. (b) Geometry of the fault plane. Asperities are depicted as gray boxes; the filled star indicates the rupture initiation point. Open stars indicate alternative rupture initiation points used in scenarios 4a–d. Numbers give the lengths of individual segments in kilometers.

reference scenario. The reference scenario is a slight modification of scenario 1a of Pulido *et al.* (2004). The tested scenarios (16 in total) are defined by changing the critical source parameters (rise time, rupture velocity, rupture initiation point, and stress drop) and attenuation parameters one at a time to observe their influence on the simulated ground motions. Following Pulido *et al.* (2004), site effects and nonlinear effects are not taken into account in this study. The comparison of the calculated earthquake scenarios provides important information about the sensitivity of the ground motions to the different source and attenuation parameters and reveals the most critical ones.

Tectonic Setting

The NAF is a ca. 1200-km-long fault structure extending through the northern part of Turkey from Erzincan in the east to the Aegean Sea in the west. The structure forms the boundary between the westward-moving Anatolian Block with respect to the Eurasian plate, accommodating the relative motion through right-lateral strike-slip motion. In the westernmost part, around the Marmara Sea, the NAF splits into two main branches (Fig. 1a). Studying Global Positioning System (GPS) displacement vectors, Okay *et al.* (2000) showed that the main strain accumulation takes place along the northernmost fault branch, which is therefore the target of our ground-motion simulations. This northernmost fault branch consists of two main segments, namely the Central Marmara fault (CMF) and the North Boundary fault (NBF). The CMF has a strike almost parallel to the general stress orientation in the region and is therefore expected to break in a pure strike-slip earthquake. The NBF, on the other hand, is oblique to the stress orientation and constitutes a releasing bend on the NAF. We therefore expect an oblique normal

mechanism along this segment. The velocity of the regional plate motion is approximately 2 cm/yr (Straub *et al.*, 1997). Major historic earthquakes along these segments of the NAF include the 1509 earthquake (M 7.2) and the 1766 earthquake sequence (M 7.1 and M 7.4). In addition, a M 6.4 earthquake ruptured along the NBF in 1963 (Ambraseys and Jackson, 2000).

Ground-Motion Simulation Methodology

We follow the approach of Pulido and Kubo (2004) and Pulido *et al.* (2004), using a hybrid method for modeling the ground motion. This procedure combines a deterministic simulation at low frequencies (0.1–1 Hz) with a semistochastic simulation at high frequencies (1–10 Hz). A finite-extent scenario earthquake source embedded in a flat-layered 1D velocity structure is assumed. The source consists of several asperities, which are divided into subfaults assumed to be point sources. The total ground motion at a given site is obtained by summing the contributions from the different subfaults. For the low frequencies, subfault contributions are calculated by using discrete wave number theory (Bouchon, 1981) and summed assuming a given rupture velocity. At high frequencies, the subfault contributions are calculated using a stochastic method that incorporates a frequency-dependent radiation pattern by applying a smooth transition from a theoretical double-couple at low frequencies to a uniform radiation pattern at high frequencies following Pulido and Kubo (2004). Point sources are summed using the empirical Green's function method of Irikura (1986). The methodology has been validated through comparison to recorded data in previous studies by Pulido and Kubo (2004) and Sørensen *et al.* (2007).

The ground-motion simulations are performed at bedrock level and therefore do not take local site effects into account. This is important to keep in mind when interpreting the simulation results because local site effects are indeed present and important, especially in the southwestern part of the city (e.g., Birgören *et al.*, 2004; Sørensen *et al.*, 2006). This issue has been addressed by Sørensen *et al.* (2006), aiming to combine ground-motion simulation results with information about local site effects.

As input for the modeling, the source needs to be defined in terms of the location of the rupturing fault and its asperities together with asperity parameters such as rise time, rupture velocity, stress drop, and seismic moment. Also the properties of the surrounding crust need to be defined through velocity structure and attenuation characteristics.

Input Scenarios

To provide a comparison between the different scenario results we have defined a reference scenario. The geometry of this scenario is shown in Figure 1b and the details are explained in the following. The location and dimension of the rupturing fault are defined by considering the local tectonics and seismicity. The debate is ongoing about whether an earthquake rupture will be able to propagate over the significant bend between the CMF and NBF segments of the NAF. Observations from several recent earthquakes show that rupture may continue across significant fault bends (for example, in the 1999 Izmit earthquake, rupture continued across the significant fault bend between the Sakarya and Karadere segments [Harris *et al.*, 2002]). Region-specific dynamic modeling has shown that both segments are likely to break when rupture initiates on the western part of the CMF, whereas a combined rupture is less likely with rupture initiation on the NBF segment (Oglesby *et al.*, 2005). Based on these results, a combined rupture cannot be excluded and we therefore follow a conservative approach and assume a combined rupture of the CMF and NBF segments. A total fault length of 130 km is used, which is confined to the area between the 1999 Izmit rupture to the east and the 1912 Ganos rupture to the west. We assume a surface-rupturing fault with a width of 20 km in agreement with the depth of the seismogenic zone as indicated by the depth distribution of seismicity (Gurbuz *et al.*, 2000). The fault-plane solution used is the one of Pulido *et al.* (2004) with pure right-lateral strike-slip faulting along the CMF and an oblique-normal mechanism along the NBF. Two asperities are defined covering 22% of the fault plane following the empirical results of Somerville *et al.* (1999). These are located near the intersection of the CMF and NBF segments (Fig. 1a). This area has previously been suggested to be a seismic gap (Gurbuz *et al.*, 2000), characterized by its low seismicity. The seismic moment released by the scenario earthquake is 2.0×10^{20} N m, which is an average value of the seismic moments estimated by different authors for the 1999 Izmit earthquake (Pulido *et al.*, 2004). The velocity model used in the modeling is the one used for routine location of earthquakes in the region (Fig. 2). For the cutoff frequency f_{max} we use a value of 10 Hz, which is also the upper-frequency limit of the calculations. In practice this implies that the high-frequency decay of the ground motion is mainly controlled by attenuation. In the computations, the fault plane is divided into subfaults with sizes of 3×3 km for the asperities and 5×5 km for the background rupture. Computations are performed for a 10-km grid spacing. This leads to a total computation time of ca. 11 hours for 276 grid points on a normal PC.

For the reference scenario, the rupture initiation point is located in the westernmost edge of asperity 1 (Fig. 1). This is believed to be a likely location because the border regions of asperities represent significant changes in physical properties of the fault and thereby zones of weakness. Based on seismic moment, fault area, and asperity area, the stress drop is calculated according to Pulido *et al.* (2004). Rupture velocity and rise time are taken from Pulido *et al.* (2004) for the reference scenario. The regional attenuation is defined in terms of a frequency-dependent Q. For the reference scenario we have used the Low Attenuation Model of Pulido *et al.* (2004). The source parameters of the reference scenario

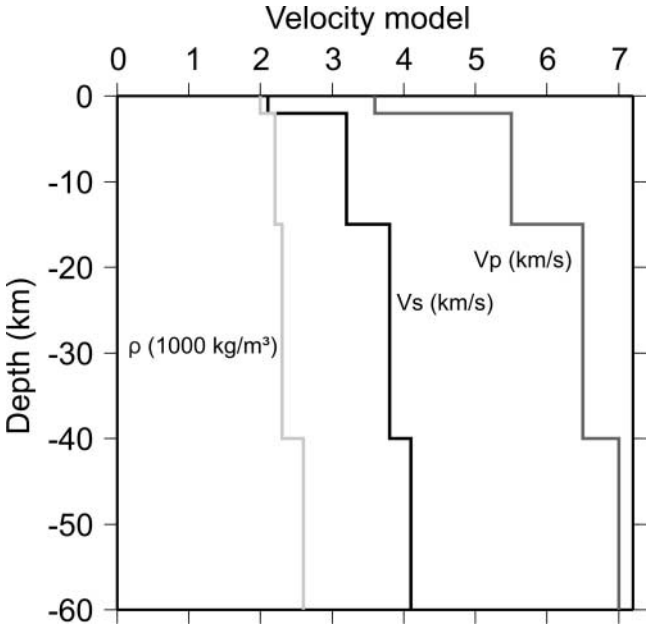

Figure 2. Velocity model for the Marmara Sea region (Serif Baris, personal comm., 2003).

are summarized in Table 1. Note that the reference scenario is considered as a conservative approximation.

Based on the reference scenario, we have changed source and attenuation parameters one by one to test their effect on the ground motions. For this purpose we simulate ground motions in the study area for each scenario and calculate their difference to peak ground acceleration (PGA) and peak ground velocity (PGV) of the reference scenario. The parameters to be tested are attenuation (Q), rise time, rupture velocity, rupture initiation point, and stress drop. In total, 16 "test scenarios" have been investigated that are listed in Table 2.

Table 1
Source Parameters for the Reference Scenario

Hypocenter (latitude/longitude/depth)	48.838° N/28.519° E/15 km
Seismic moment	$2.0 \cdot 10^{20}$ N m
Strike/dip/slip CMF segment	81.5/90/180
Strike/dip/slip NBF segment	110/90/−135
Average stress drop	5 MPa
Asperity stress drop	10 MPa
Rise time	3.0 sec
Rupture velocity	3.0 km/sec
f_{max}	10 Hz
Q	$100 \cdot f^{1.5}$

Table 2
Scenarios Tested in This Study

Scenario 1a	$Q = 100 \cdot f^{0.5}$
Scenario 1b	$Q = 250 \cdot f^{1.5}$
Scenario 1c	$Q = 250 \cdot f^{0.5}$
Scenario 2a	Rise time, 2.0 sec
Scenario 2b	Rise time, 4.0 sec
Scenario 2c	Rise time random, 3 ± 1 sec
Scenario 3a	Rupture velocity, 2.5 km/sec
Scenario 3b	Rupture velocity, 3.5 km/sec
Scenario 3c	Rupture velocity random, 3 ± 0.5 km/sec
Scenario 4a	Rupture initiation at intersection of CMF and NBF
Scenario 4b	Rupture initiation at eastern edge of asperity 2
Scenario 4c	Rupture initiation at eastern edge of NBF
Scenario 4d	Rupture initiation at western edge of CMF
Scenario 5a	Stress drop asperity, 5 MPa; background, 2.5 MPa
Scenario 5b	Stress drop asperity, 15 MPa; background, 7.5 MPa
Scenario 5c	Stress drop ratio, 0.05

Only the parameters differing from the reference scenario are listed.

Simulation Results

The simulated PGA and PGV values for the reference scenario, taken as the maximum value of the horizontal components, are shown in Figure 3. The largest accelerations are predicted in the southernmost part of Istanbul, which is also located closest to the rupturing fault. Here we can expect bedrock accelerations of 500 cm/sec^2 or more in some places. There is a very strong forward directivity effect on the ground motions, which is especially evident in the PGV distribution. Largest velocities are expected in the southeastern part of the city, where we predict velocities up to 125 cm/sec. Because of the forward directivity, the shaking is extended far toward the east from the rupturing fault, which may have important implications along the populated areas around the Izmit gulf. The very high ground motions observed near the asperities (especially for velocity) are because of the surface-breaking nature of the earthquake. If the fault is buried just a few kilometers, these values are significantly reduced whereas ground motions away from the fault are little affected.

The results of the test scenarios are discussed in the following sections. For each tested parameter, a joint figure has been produced showing the absolute deviation of PGA and PGV from the reference scenario for each test. The color scale in each figure is scaled after the maximum difference observed for the given parameter. Regions with observed variations of less than 5% of the maximum are shown as yellow. The ground motion distribution for each scenario and individually scaled figures showing deviation of PGA and PGV from the reference scenario are provided in the Ⓔ electronic edition of BSSA.

Variability in Q

In scenarios 1a, 1b, and 1c we have tested the effect of attenuation by varying Q (Fig. 4). In the ground motion simulations we use a frequency-dependent Q defined by a relationship of the form $Q = Q_0 \cdot f^a$. In scenario 1a, we change the frequency dependency of the attenuation, coefficient a, using $a = 0.5$ ($a = 1.5$ for the reference scenario). This implies lower values of Q for the higher frequencies, which implies higher attenuation of the seismic waves. For scenario 1a, we

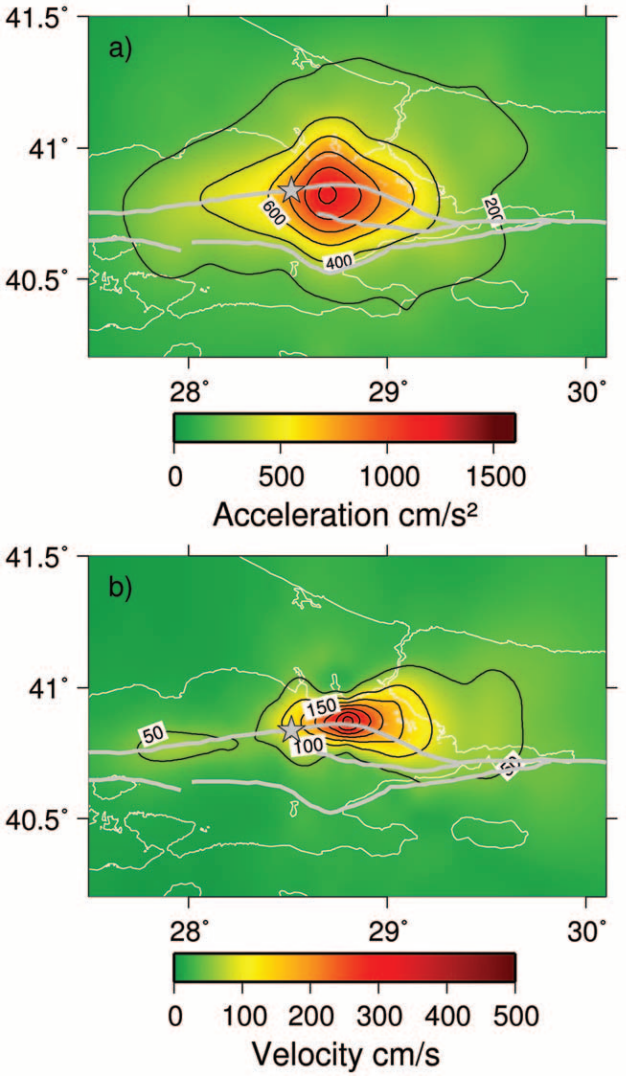

Figure 3. Simulation result for the reference scenario. (a) PGA distribution; (b) PGV distribution. Major faults are shown as gray lines, and the rupture initiation point as a star.

see a reduction of PGA over a large area with a magnitude of up to 350 cm/sec^2 in comparison to the reference scenario. For the PGVs, the effect is smaller (maximum difference of 35 cm/sec compared to reference scenario), but there is a tendency of increased PGVs in the forward directivity direction and decreased PGVs in the backward directivity direction. In scenario 1b we increase Q_0 to a value of 250 (Q_0 = 100 for the reference scenario). This causes a general increase of Q, which implies reduced attenuation. We observe a slight increase in PGA over the study area with a magnitude of up to 70 cm/sec^2. The effect on PGV is similar to the effect observed in scenario 1a. This is as one would expect because both scenarios represent an increase in Q for the lower frequencies affecting mainly PGV. For the sake of comparison we have defined a scenario (scenario 1c) by combining scenarios 1a and 1b ($Q = 250 \cdot f^{0.5}$) (Fig. 4). The effect of using this attenuation relation is expectedly a combination of the previously mentioned results. The PGA is reduced over the entire study area, but this reduction is less pronounced than for scenario 1a (up to 150 cm/sec^2). For PGV, a pattern as described for scenarios 1a and 1b is seen with slightly larger magnitude in the forward directivity direction where PGV increases with up to 50 cm/sec.

Variability in Rise Time

In scenarios 2a–c (Fig. 5), the influence of the rise time on the ground motion was tested by simulating ground motions with constant rise times of 2 sec (scenario 2a) and 4 sec (scenario 2b), and with randomly varying values between 2 and 4 sec (scenario 2c), and comparing with the reference scenario with a rise time of 3 sec. A uniform distribution was used for the randomization of the rise time. The effect of the rise time on PGV is clear. Increasing the rise time decreases the PGV and vice versa. The effect is most dominating in regions adjacent to the asperities where we see a change of up to $\pm$170 cm/sec relative to the reference scenario. The effect of using a randomly varying rise time is negligible (change less than 5 cm/sec in the entire study area). The effect on the PGAs is more scattered and diffuse. The general trend is a scattered reduction in PGA for both reduced and increased rise time with the largest impact in regions adjacent to the asperities. Letting the rise time vary randomly also causes a reduction in PGA. In all cases, the maximum level of change is 500–600 cm/sec^2.

Variability in Rupture Velocity

In scenarios 3a–c, the effect of the rupture velocity has been tested (Fig. 6). In scenario 3a, the rupture velocity was reduced to 2.5 km/sec (3.0 km/sec for the reference scenario), in scenario 3b it was increased to a supershear velocity of 3.5 km/sec, and in scenario 3c we let the rupture velocity vary randomly between 2.5 and 3.5 km/sec. A uniform distribution was used for the randomization of the rupture velocity. The simulation results show that the rupture velocity has a strong effect on the PGVs, especially in the forward directivity direction. Increasing the rupture velocity also increases the PGV, whereas a reduction in rupture velocity causes reduced PGVs. The supershear rupture velocity used in scenario 3b leads to a focusing of the ground motion at the parts of the asperities closest to the hypocenter. This may explain the reduction in PGV near the fault bend. This effect is even stronger using a higher rupture velocity of 5 km/sec (not presented here), which is at the order of what was observed for the 1999 Izmit earthquake (Bouchon *et al.*, 2001). Using the randomly varying rupture velocity causes a reduction of the PGV over an extended area. The level of change for the PGV is up to 150 cm/sec. A similar effect is seen for the PGAs. Reduction of rupture velocity reduces the PGAs, whereas increased rupture velocity causes increased PGA. Using a random rupture velocity has a minor effect on

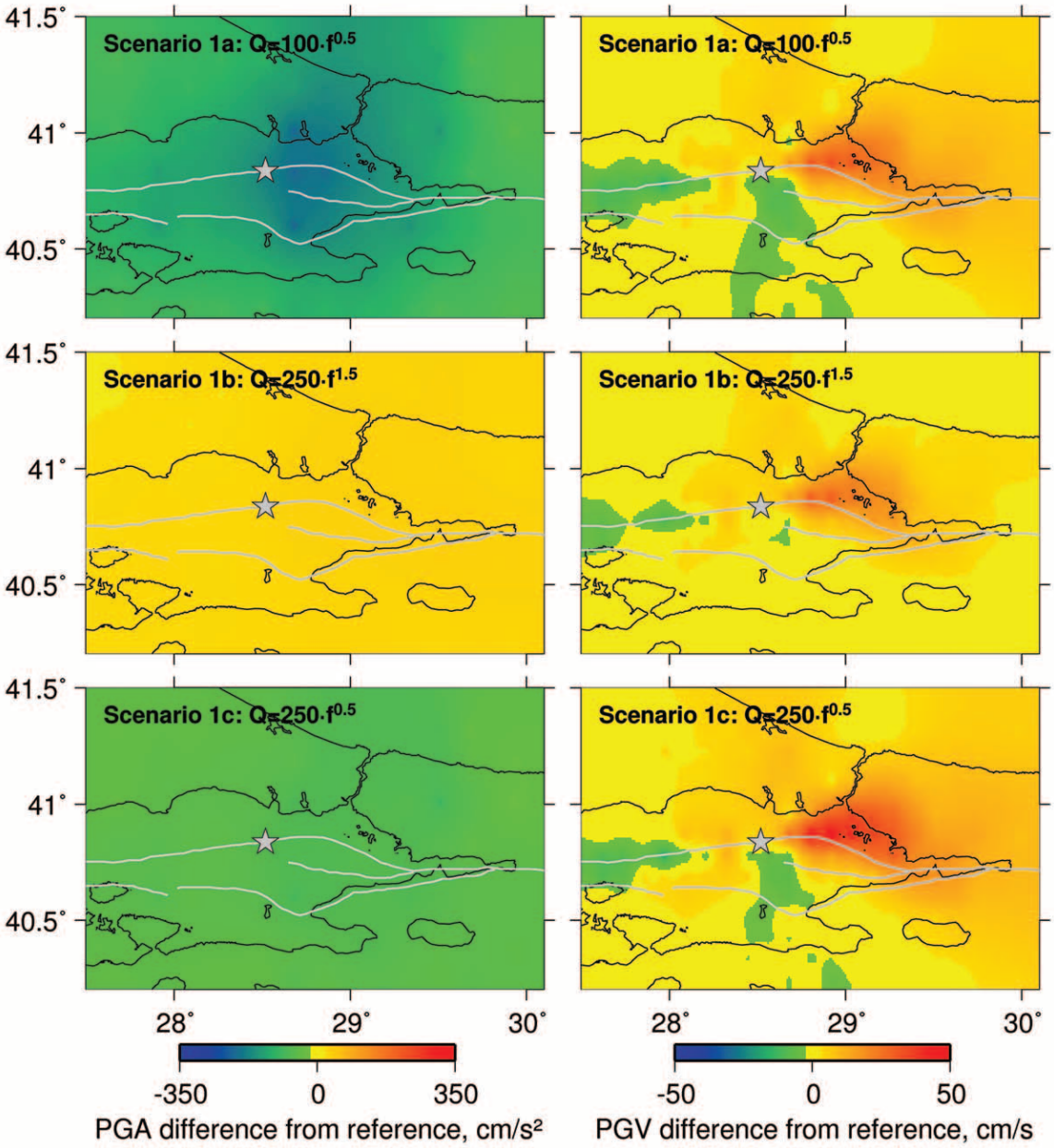

Figure 4. Simulation results for scenarios 1a–c where the effect of attenuation is tested. The plots show the absolute difference in the ground-motion values compared with the reference scenario. Major faults are shown as gray lines and the rupture initiation point is shown as a star.

the PGA values. The level of maximum change for the PGAs is 600–700 cm/sec^2.

Variability in Rupture Initiation Point

The effect of changing the location of rupture initiation has been tested in scenarios 4a–d (Fig. 7). In scenario 4a, the rupture initiation point (RIP) was moved to the intersection of the CMF and NBF segments of the rupturing fault. In scenario 4b, the RIP was located at the easternmost point of asperity 2, and for scenario 4c the RIP was located at the easternmost point of the NBF segment. In scenario 4d, the RIP was moved westward to the westernmost point of the CMF. For all these scenarios, the hypocentral depth was held constant at 15 km for easy comparison. The simulation results show a clear effect of the location of the RIP on the distribution of the ground motion. For the PGVs, the effect of directivity is very clear and significant. For scenario 4a we see a reduction of PGV in the forward directivity direction of the reference scenario due to the changed direction of rupture propagation along asperity 1. This also causes an increase in PGV toward the west. The same trend is seen

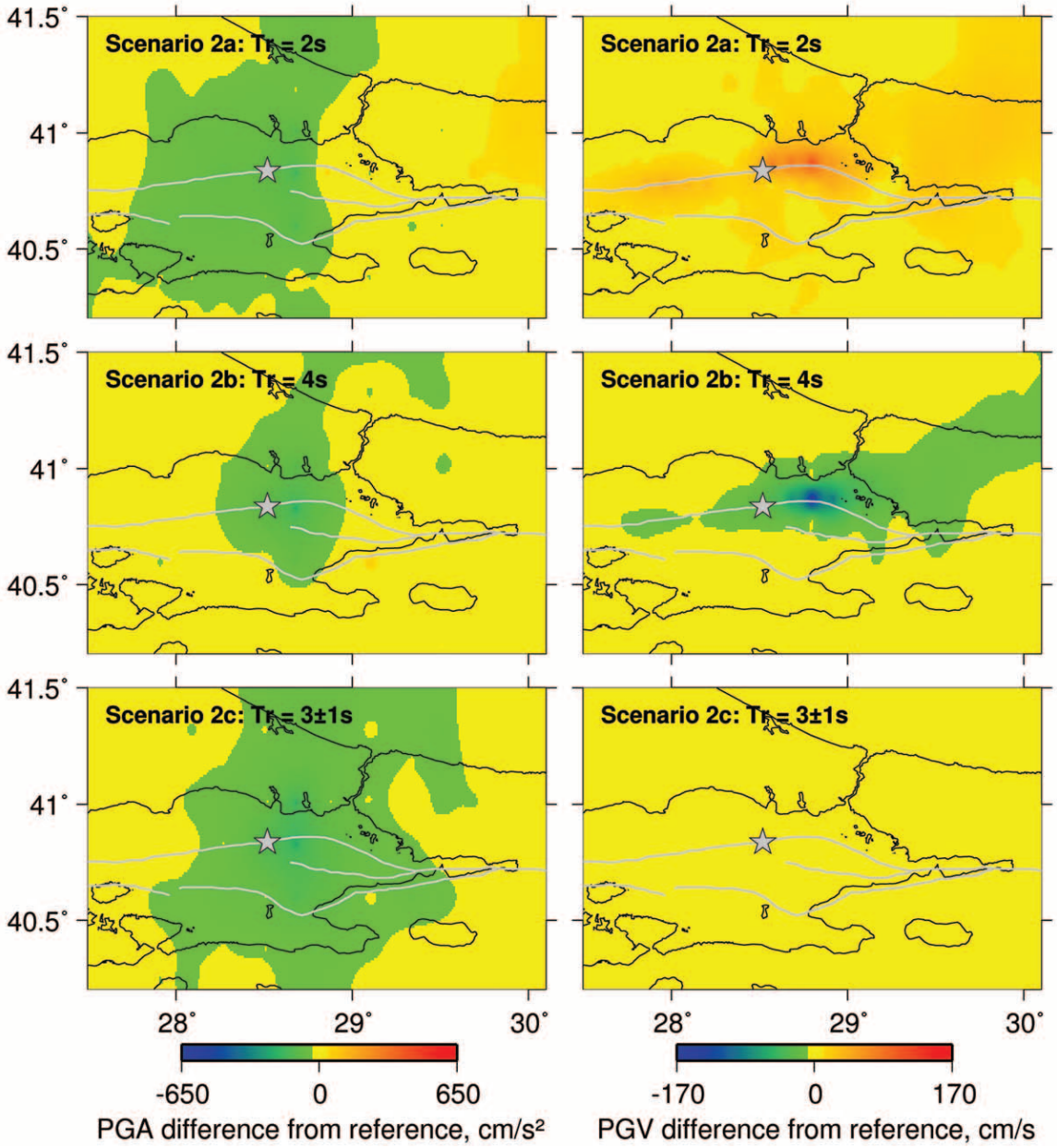

Figure 5. Simulation results for scenarios 2a–c where the effect of rise time is tested. The plots show the absolute difference in the ground-motion values compared with the reference scenario. Major faults are shown as gray lines and the rupture initiation point is shown as a star.

more clearly for scenarios 4b and 4c where the RIP is moved successively further eastward. This completely changes the directivity pattern, causing reduced PGVs to the east and increased PGVs to the west. For scenario 4d, moving the RIP westward has a small effect on the simulated ground velocities. The magnitude of the change is up to 300 cm/sec in all cases except scenario 4d where PGV changes on the order of 100 cm/sec. For the PGA distribution, the same trend is present, but with more scatter due to the more incoherent nature of accelerations. For scenario 4d we observe a slight decrease in PGA close to the epicenter due to the directivity toward this region in the bilateral rupture of the reference scenario. The maximum magnitude of the variation varies between 400 and 700 cm/sec^2 for the four scenarios. Scenarios 4a, 4c, and 4d are equivalent of scenarios 3, 2, and 1a of Pulido *et al.* (2004), respectively. The variation among scenarios presented by Pulido *et al.* (2004) is in agreement with the scenarios shown in Figure 7. This confirms the strong effect of the location of rupture initiation on the directivity of the ground-motion distribution.

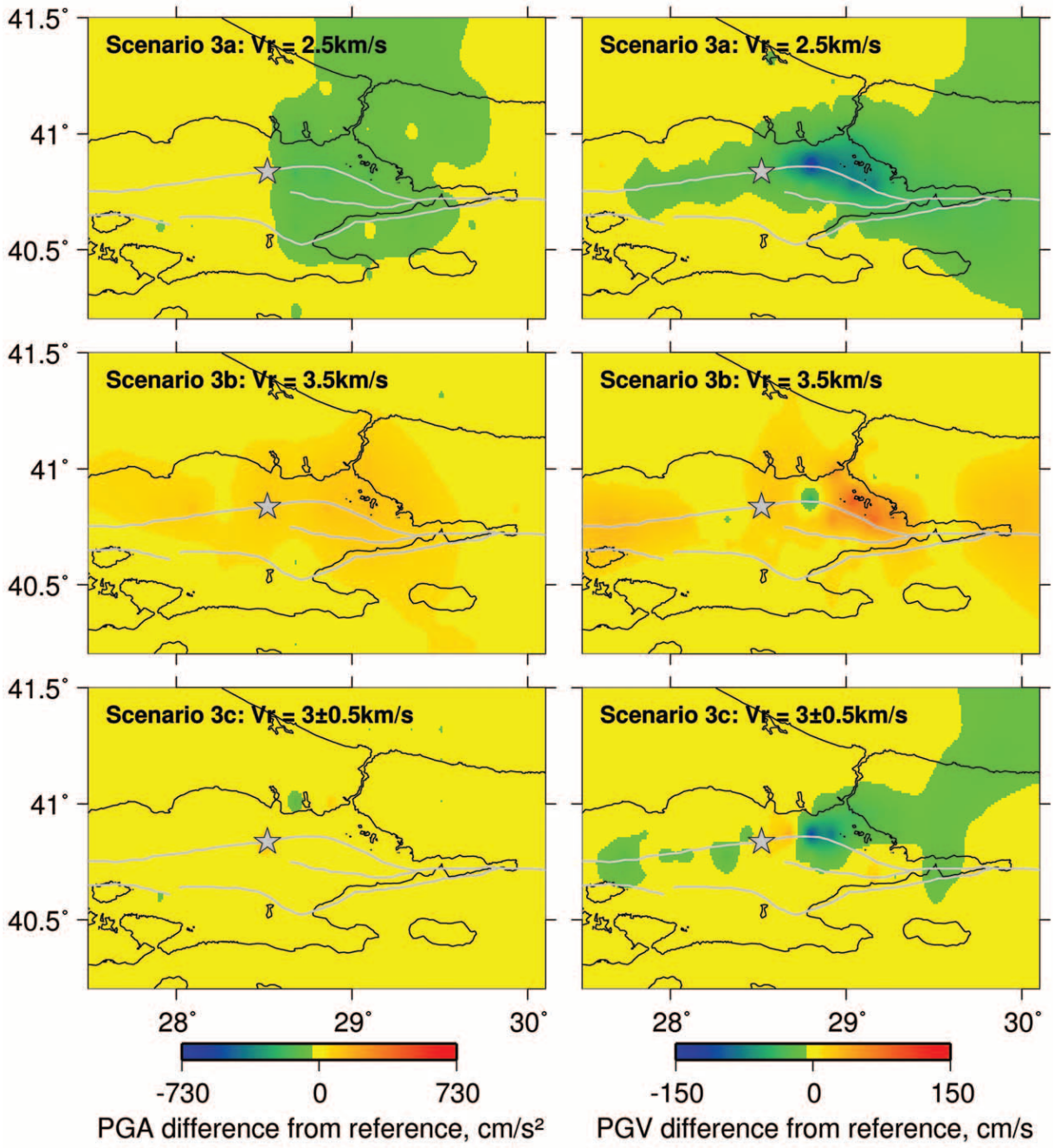

Figure 6. Simulation results for scenarios 3a–c where the effect of rupture velocity is tested. The plots show the absolute difference in the ground-motion values compared with the reference scenario. Major faults are shown as gray lines and the rupture initiation point is shown as a star.

Variability in Stress Drop

The final test of this study was for the influence of stress drop on the ground-motion distributions in scenarios 5a–c (Fig. 8). In scenario 5a, the stress drop was reduced by 50% to 2.5 MPa for the background slip and 5 MPa for the asperities. In scenario 5b, the stress drop was increased by 50% to 7.5 MPa for the background slip and 15 MPa for the asperities. Both of these scenarios have a stress-drop ratio (background/asperity) of 0.5 as used also for the reference scenario. This is based on the results of Das and Kostrov (1986) that stress-drop ratio scales with the ratio of background fault radius to asperity radius (for details, see Pulido *et al.*, 2004). More recent results by Dalguer *et al.* (2004) indicate, based on dynamic rupture models, that much lower stress-drop ratios (less than 0.05) are needed to fit observations from actual earthquakes. To test the effect of reducing

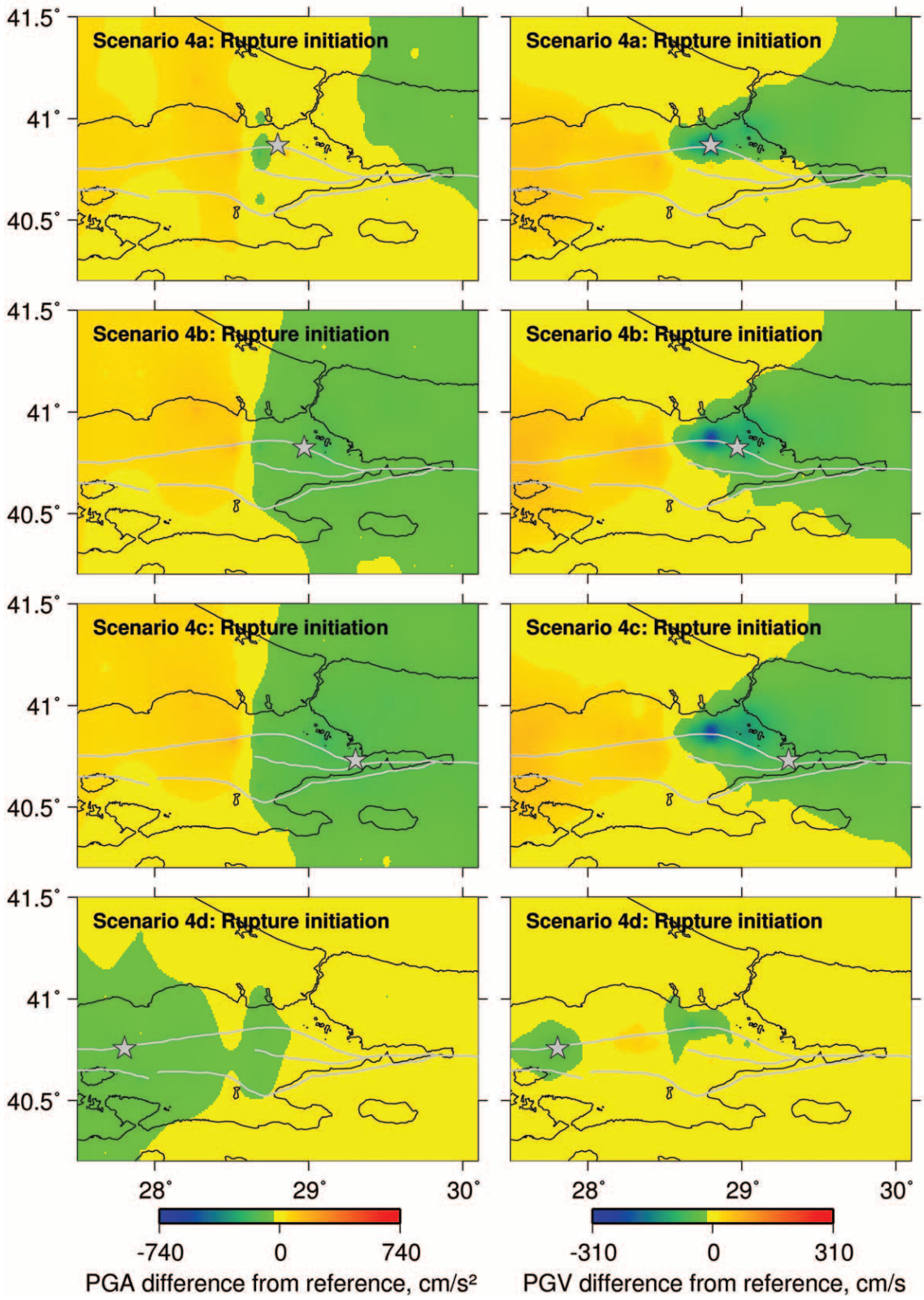

Figure 7. Simulation results for scenarios 4a–d where the effect of rupture initiation point is tested. The plots show the absolute difference in the ground-motion values compared with the reference scenario. Major faults are shown as gray lines and the rupture initiation point is shown as a star.

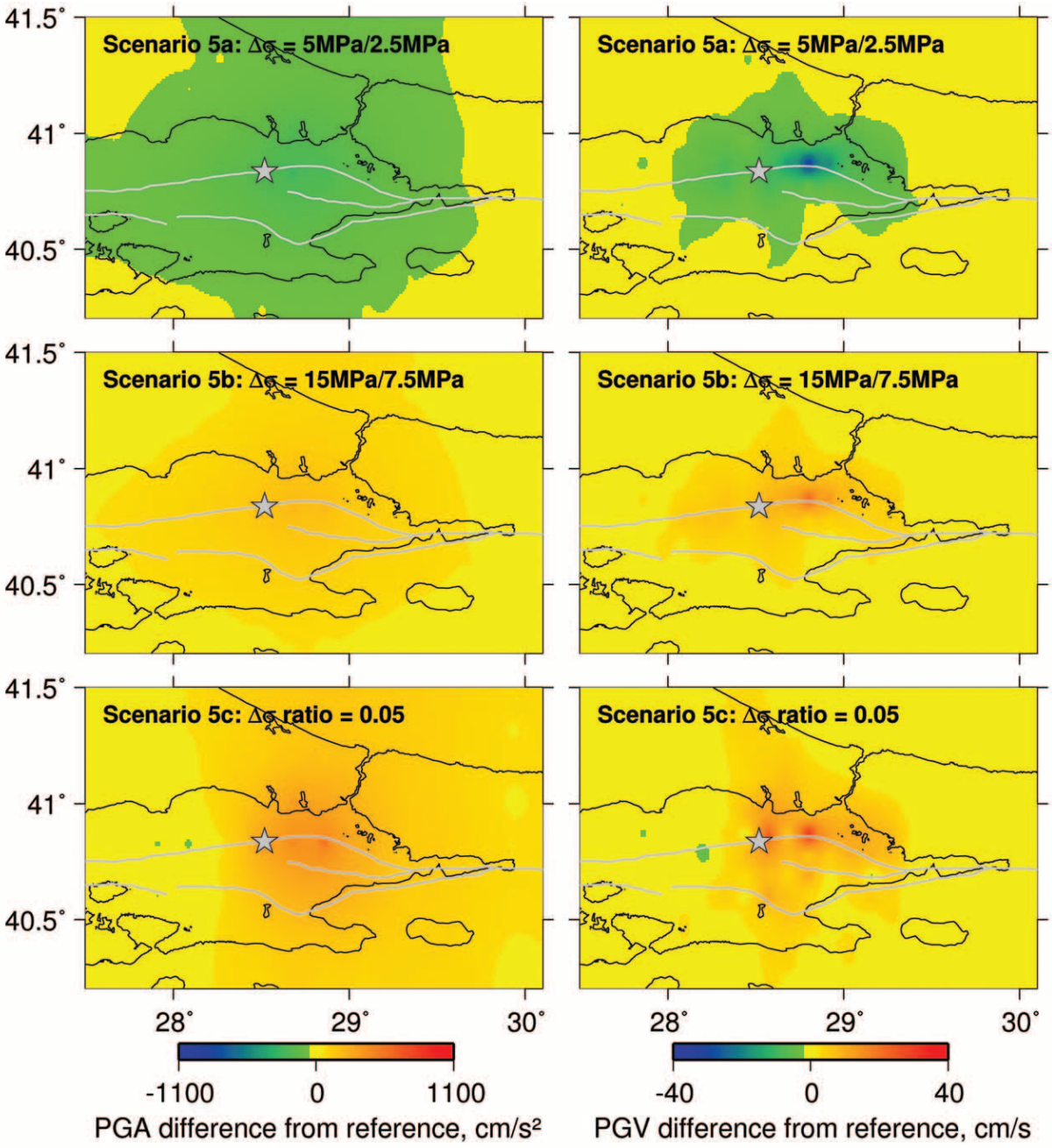

Figure 8. Simulation results for scenarios 5a–c where the effect of stress drop is tested. The plots show the absolute difference in the ground-motion values compared with the reference scenario. Major faults are shown as gray lines and the rupture initiation point is shown as a star.

the stress-drop ratio, a third scenario, scenario 5c, was tested with a stress-drop ratio of 0.05, maintaining the average stress drop of the reference scenario (6.1 MPa). This implies an asperity stress drop of 24 MPa. The effect of varying the stress drop is most significant on the PGA levels, which is reasonable because stress drop is only included directly in the high-frequency part of the calculations. Both PGV and PGA decrease when decreasing the absolute level of stress drop and increase for an increased stress drop, affecting a larger area around the rupturing fault for PGA. Reducing the stress drop ratio leads to a very strong increase in the ground motion near the asperities. The increased ground motions are spread over a large area in the direction of forward directivity. A decrease in ground motion is observed on the fault segment to the west of the epicenter. This is due to the decreased stress drop on this background fault segment outside the direction of forward directivity. Reducing the stress-drop ratio further, using a ratio of 0 (i.e., zero stress drop at

the background fault segments) leads to a very similar ground-motion distribution. The magnitude of the change in ground motion is 30–40 cm/sec for PGV and up to 1100 cm/sec^2 for PGA when varying the stress-drop ratio. Changing the absolute level of stress drop leads to changes in PGA up to 500 cm/sec^2.

Comparison of Parameters

As shown in the previous sections, several of the input parameters used in the ground-motion simulations have a significant effect on the resulting ground motions, both in terms of distribution and absolute level of the ground motions. The location of the rupture initiation is critical because of the effects of directivity and, for the case of Istanbul, it controls the distribution of very strong shaking in the densely populated areas of the city center vs. offshore in the Marmara Sea.

The magnitudes of changes caused by varying the rise time and rupture velocity are at the same level. However, the nature of the changes are different in terms of the affected regions. The effect of rise time is mainly observed in regions adjacent to the asperities where most of the slip occurs, but also tends to distribute in the direction of rupture propagation. The rupture velocity, on the other hand, has an important effect along the whole rupture and the largest variations are seen along the forward directivity direction. In both cases the effect on PGA is scattered and, in general, distributed over larger regions than the PGVs.

Figure 9 shows the distribution of standard deviations in PGA and PGV based on all 17 scenarios. In general, these two maps indicate that the largest variation in the standard deviation occurs close to the asperities. This is as expected because much of the variation in the ground motion is associated with the location of asperities and their input parameters. Their variation naturally affects the surrounding regions. The level of standard deviation of both PGA and PGV decreases gradually with increasing distance from the fault asperities. However, PGA variability is spread over a wider area than PGV variability.

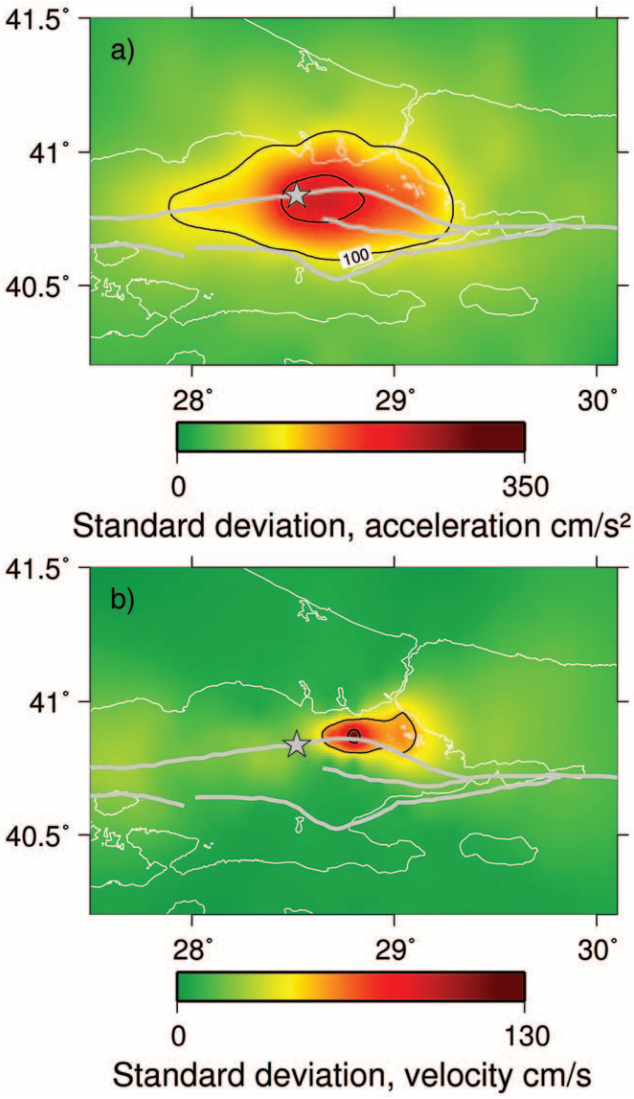

Figure 9. Spatial distribution of standard deviation of PGA (a) and PGV (b) based on the 16 scenarios. Major faults are shown as gray lines, and the rupture initiation point as a star.

Frequency Distribution of Ground Motion and Implications for Engineering

When applying seismic-hazard results to engineering problems, the frequency distribution of the ground motion becomes an important factor in addition to the peak ground motion. Therefore we have studied the frequency distribution of the ground-motion simulation results at six sites in terms of spectral velocity (SV) and response spectra. The locations of the sites (Fig. 1a) have been chosen to represent different parts of the city both in terms of land use, local geology, and directivity of the simulated ground motions. Site PEN (Pendik) is located on the Asian side of the city in the forward directivity direction for the reference scenario. Site KUM (Kumköy) is north of the city at the Black Sea coast and is included for investigating the effect of distance on the spectra. Sites SIT (Avcilar) and ATA (Ataköy) are located in areas known to be affected by local site effects (Tezcan *et al.*, 2002; Sørensen *et al.*, 2006). The remaining two sites, HIS and BUS, are located in the historical center (Sultanahmet) and the business center (Levent), respectively. As an example, the simulated waveforms for the reference scenario at site ATA are shown in Figure 10.

For each of the six sites, SV has been averaged in three frequency bands, namely $f < 1$ Hz, 1 Hz $< f <$ 5 Hz and $f > 5$ Hz. The limits of these frequency bands are chosen to coincide with the spectrum characteristic periods of the Turkish Design Code for various site classes (Aydinoglu, 1998). A large part of the building stock in Istanbul consists of three- to five-story buildings with resonance frequencies at about 3–5 Hz. However, numerous medium-rise buildings susceptible to frequencies down to 1 Hz are also present.

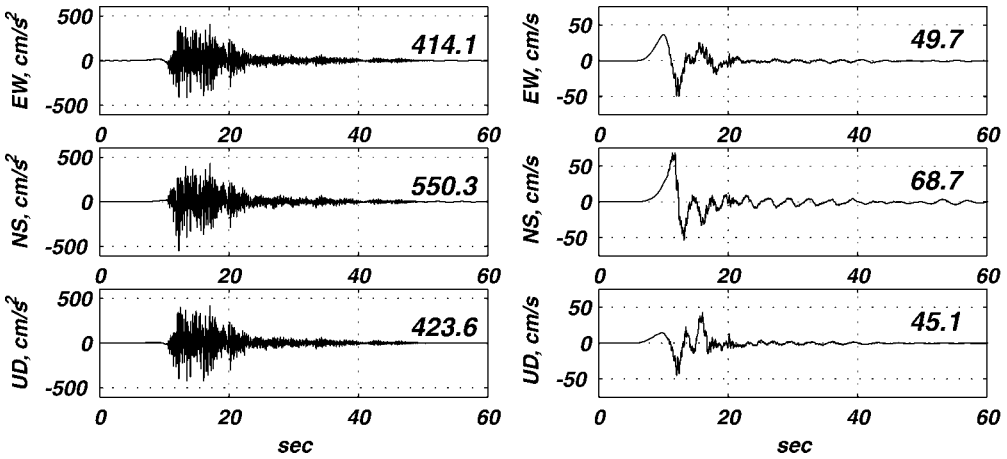

Figure 10. Simulated waveform for the reference scenario at site ATA (for location, see Fig. 1a). Acceleration time histories are shown to the left, velocities to the right. Numbers above the traces give the maximum amplitude for each trace.

Shaking at frequencies lower than 1 Hz mainly affects high-rise or long-span structures (which may also be vulnerable to higher frequencies depending on their modal shape) and therefore has less engineering implications in most parts of the city. Figures 11–13 show the comparisons of spectral values for each of the six sites. For each site, average SVs are computed for the reference scenario and each of the 16 test scenarios, and the absolute values are compared.

For the low frequencies (Fig. 11), the most dominating parameters are rise time, rupture velocity, and location of the RIP (scenarios 2a–c, 3a–c, and 4a–d). The influence of the rise time is significant at all the sites, whereas rupture velocity and RIP have little effect at the northernmost site (KUM), indicating that the effect of these parameters is mainly significant within a short distance to the fault.

In the 1- to 5-Hz frequency band (Fig. 12), the most remarkable effect on spectral values is coming from variations in the stress drop (scenarios 5a–c). We also see an effect of the RIP and the frequency dependence of the attenuation (scenario 1a) on the spectral values.

In the highest frequency band (Fig. 13), the main variations are due to the frequency dependence of the attenuation and the stress drop. The effect of the RIP is also visible in this frequency band, but not as pronounced as for the lower frequencies.

The observations from Figures 11–13 provide us with the following information about the parameters: Rise time and rupture velocity have their main effect on the low-frequency ground motions despite their use in both the low- and high-frequency calculations. This implies that even though these parameters cause large variations in the ground-motion levels; their effect for engineering issues is limited in most parts of the town. The location of rupture initiation affects all frequencies, but the effect decreases for increased frequencies, indicating that the RIP mainly has an impact on the damage of large structures such as high-rise buildings. The stress drop, and especially the stress-drop ratio (asperity to fault average stress drop), affects all ground motions above 1 Hz (the parameter is only introduced directly for the high-frequency calculations) and thereby it is an important parameter with large impact on the level of potentially damaging ground motion, which should be given attention in future studies. The attenuation (Q) is another parameter only introduced for the high-frequency computations. The main effect on the ground motion is due to varying the frequency dependence, and this effect increases for increasing frequency as one would expect. For the low frequency computations, attenuation is introduced through Q_p and Q_s in the velocity model. The effect of varying these parameters has shown to be negligible (not presented here).

In Figures 11–13, the SV values are plotted for the east–west and the north–south components separately. For the high frequencies ($f > 5$ Hz), the amplitudes are almost identical for the two components, which is in agreement with the radiation pattern correction applied in the simulations (isotropic radiation pattern at high frequencies). However, at lower frequencies large differences are seen, especially in the forward directivity direction (PEN), which are probably a combined effect of the directivity and the double-couple radiation of the low-frequency energy from the fault.

Response Spectra in Istanbul

Figure 14 shows velocity response spectra for the 17 scenarios at the six sites of Figure 1a. It is seen that both peak frequency and spectral level varies with azimuth and distance to the fault. The response spectra of the reference scenario are shown in the figure as black lines. At PEN (Fig. 14a) we see a very strong peak at low frequencies in the north–south direction. This is expected to be due to the forward directivity of the ground motion. In general, at this site, we see maximum response-spectral values at 0.1- to 0.2-Hz

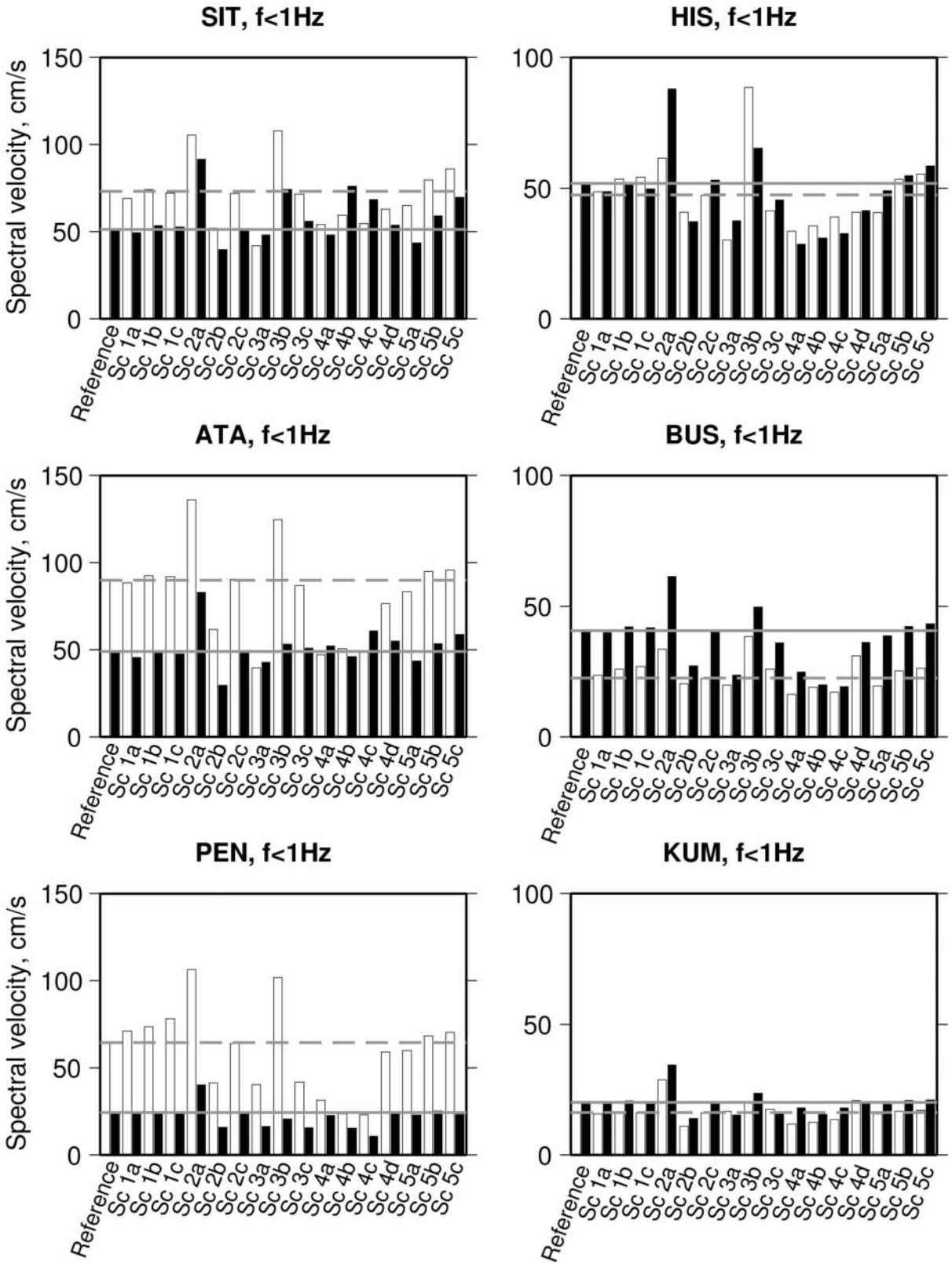

Figure 11. Average spectral velocity at the sites in Figure 1a in the frequency band $f < 1$ Hz. Open bars represent the north–south component of the ground motion and filled bars represent the east–west component. The gray lines indicate the spectral level for the reference scenario: the solid line for the east–west component and the dashed line for the north–south component. Note the different scales for the sites.

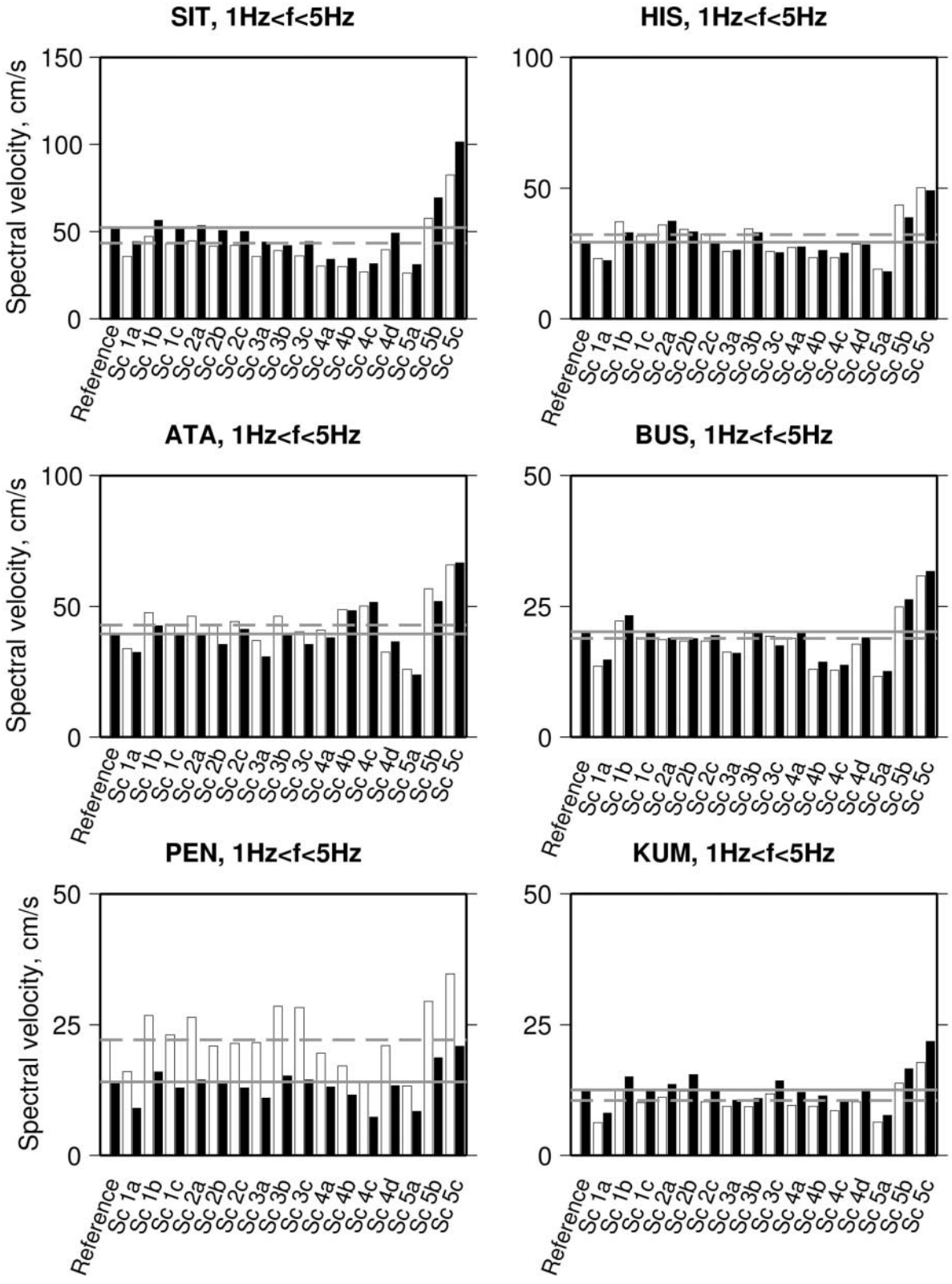

Figure 12. Average spectral velocity at the sites in Figure 1a in the frequency band 1 Hz $< f <$ 5 Hz. Open bars represent the north–south component of the ground motion and filled bars represent the east–west component. The gray lines indicate the spectral level for the reference scenario: the solid line for the east–west component and the dashed line for the north–south component. Note the different scales for the sites.

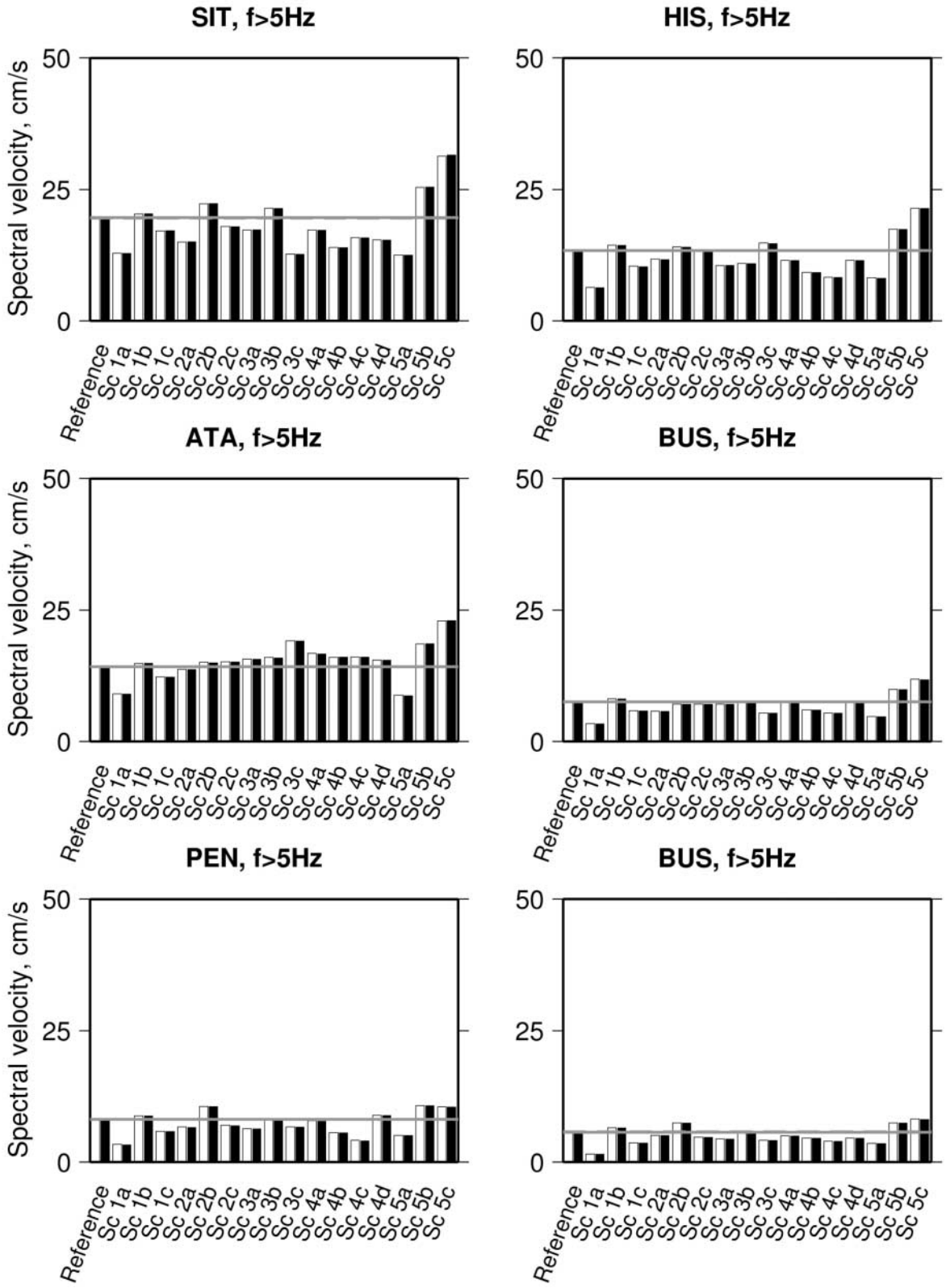

Figure 13. Average spectral velocity at the sites in Figure 1a in the frequency band $f > 5$ Hz. Open bars represent the north–south component of the ground motion and filled bars represent the east–west component. The gray lines indicate the spectral level for the reference scenario: the solid line for the east–west component and the dashed line for the north–south component.

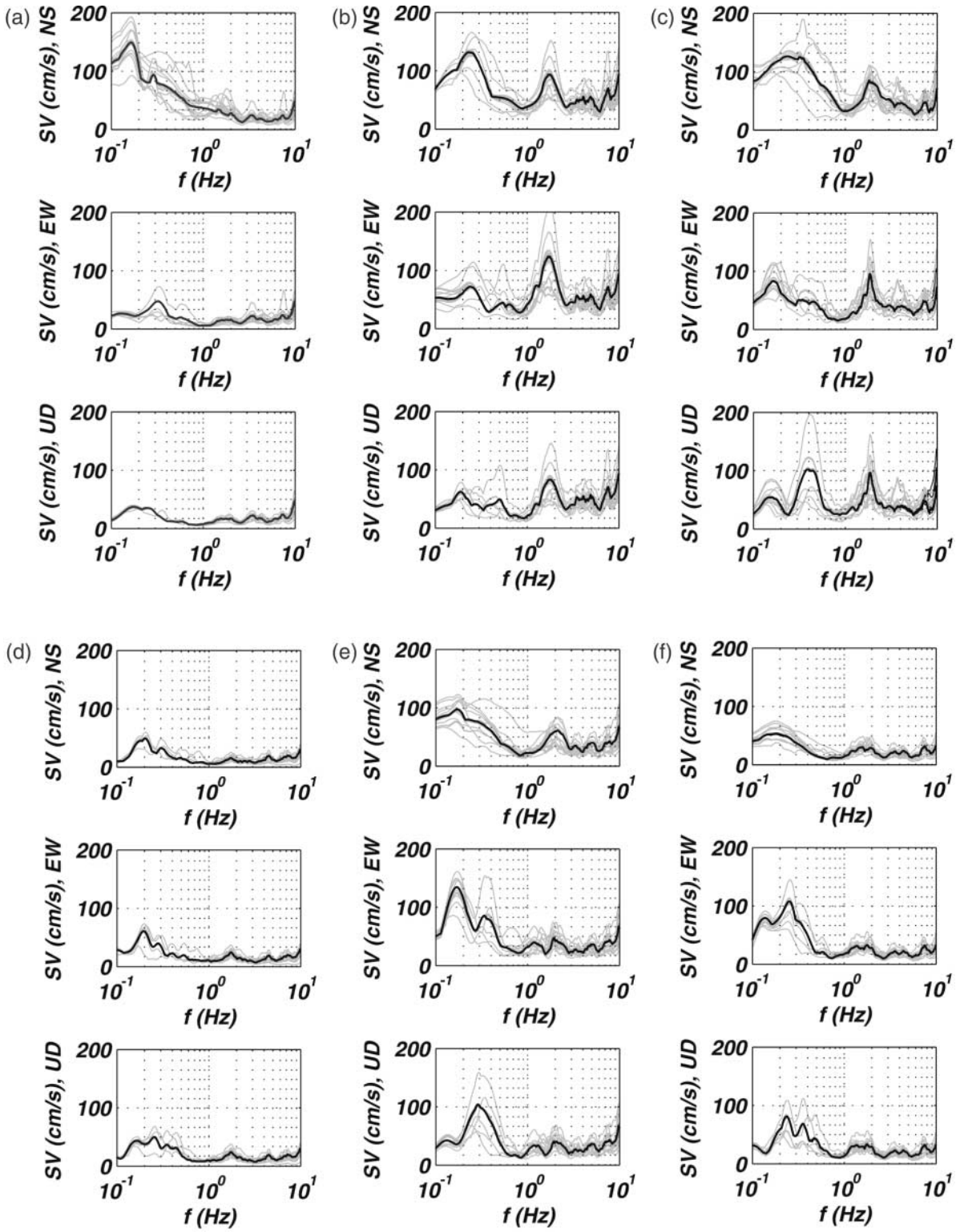

Figure 14. Comparison of 5% damped velocity response spectra for all 17 scenarios. The reference scenario is shown as a thick black line. All three components are shown. The various test scenarios are not differentiated in the plot since the aim is to show the variation and the upper and lower bounds of the spectra. (a) PEN; b) SIT; (c) ATA; (d) KUM; (e) HIS; (f) BUS.

frequencies, which will have an effect on high-rise buildings in this area. Secondary peaks are seen around 2 Hz and 4 Hz, which will have a smaller absolute effect, but will affect lower-rise buildings, which are more common.

The response spectra for SIT and ATA (Fig. 14b and c) are very similar and differ significantly from the spectra at PEN. For these spectra we see a strong peak at about 2 Hz which is due to directivity effects (forward and backward) for the rupture. This peak is especially strong for these stations, which are affected the most by directivity, but is also observed at many other stations. The peak will be very critical for building damage in these densely populated areas largely occupied by ~5 story buildings, which have resonance frequencies around this value (Aydinoglu, 1998). Since we expect significant site effects in this area with amplification also around this frequency (Sørensen *et al.*, 2006), the actual response can be even higher than predicted in this study. Again we also see peaks around 0.2 and 0.5 Hz which can affect high-rise buildings.

KUM (Fig. 14d) is located far from the rupturing fault, which is also reflected in the response spectra having significantly lower values. The dominating peak is at low frequencies, 0.2–0.3 Hz, but here amplitudes are also low and little effect is predicted.

At HIS (Fig. 14e), the Sultanahmet site, we also see a main peak at 0.2 Hz and a strong secondary peak at 2 Hz. This secondary peak will be critical for the building stock mainly consisting of old residential blocks of about five stories. The many historical monuments have much more complex response than simple quadratic modern residential buildings and may be vulnerable to a variety of frequency bands.

Finally, for the site BUS (Fig. 14f) located in the business district of Istanbul, the strongest velocity response is seen at low frequencies (0.2–0.3 Hz), which is critical for the many high-rise buildings (40 stories and more) present in this area.

From an engineering perspective, an important result of the sensitivity analysis of this study is the effect of changing the scenario input parameters on the resulting response spectra. Despite the large variations between the various scenarios in terms of ground-motion level and distribution, the response spectra shown in Figure 14 are similar for most scenarios. The general trend is that the variation increases for the low frequencies. For the peak frequencies we see a significant variation up to $\pm$ 50%, but this is only seen for a few scenarios involving changes in rupture velocity and rise time. In general, the variation between the response spectra is larger for sites close to the fault (SIT and ATA in Fig. 14b and c), whereas much smaller variations are seen at larger distances (KUM and BUS in Fig. 14d and f).

Figure 15 shows the distribution of standard deviation of the response spectra in three frequency bands based on the 17 scenarios. For the spectral accelerations (Fig. 15a–c) there is a strong frequency dependence of the standard deviations. At the low and intermediate frequencies ($f < 5$ Hz) standard deviation is small, whereas there is a remarkable variation between the scenarios for the high frequencies. For $f > 5$ Hz, standard deviations of up to 1000 cm/sec^2 are observed in the acceleration response spectra, and significant variation is distributed over a large area. For the velocity response spectra (Fig. 15d–f), the standard deviation decreases rapidly with distance to the fault with a maximum spectral standard deviation of 10–15 cm/sec in southern Istanbul. We see that the main variability in the standard deviation of velocity response spectra is associated with the low frequencies ($f < 1$ Hz). The similarity between the response spectra at low and intermediate frequencies implies that even if we are uncertain of the exact values of the input parameters for ground-motion modeling, we still do a reasonably good job in predicting consistent response spectra up to frequencies at about 5 Hz. However, the large variation observed for frequencies above 5 Hz, though less important in engineering applications, cannot be ignored.

Discussion

The results of this study reveal that even if we have reliable ground-motion estimation methodologies we are still limited in the prediction of ground motions from future earthquakes by our limited knowledge of the source and attenuation parameters. This uncertainty is important and should always be kept in mind when interpreting ground-motion simulation results. However, being aware of the uncertainties, ground-motion simulations still provide a strong tool in determining seismic-hazard levels in places with a high probability of exceedence.

The current study has provided some bounds for the uncertainties related to the input parameters, information that can hopefully be used in the future to provide more reliable seismic-hazard estimates. Table 3 summarizes the average standard deviations of the different ground-motion measures and their coefficient of variance (CV, standard deviation normalized by the mean) based on all simulation sites. Here, the preceding observations that the most stable ground-motion measures are the low-frequency spectra are confirmed. The average standard deviations of all ground-motion measures are less than 35% of the mean.

When modeling ground motions from future earthquakes, one approach for dealing with the uncertainties is to define several scenarios with different values of the uncertain source parameters. For example, a "worst-case scenario" and a "best-case scenario" can be defined. In this way, upper and lower limits of the expected ground motions can be defined and the user can choose the appropriate level of conservatism depending on the use of the results. Furthermore, comparison of calculated spectra with existing regional design spectra and of calculated peak ground motions with attenuation relations (as done by Pulido *et al.*, 2004) can provide important information about the performance of the ground-motion simulation technique and the hazard level due to the scenario earthquake.

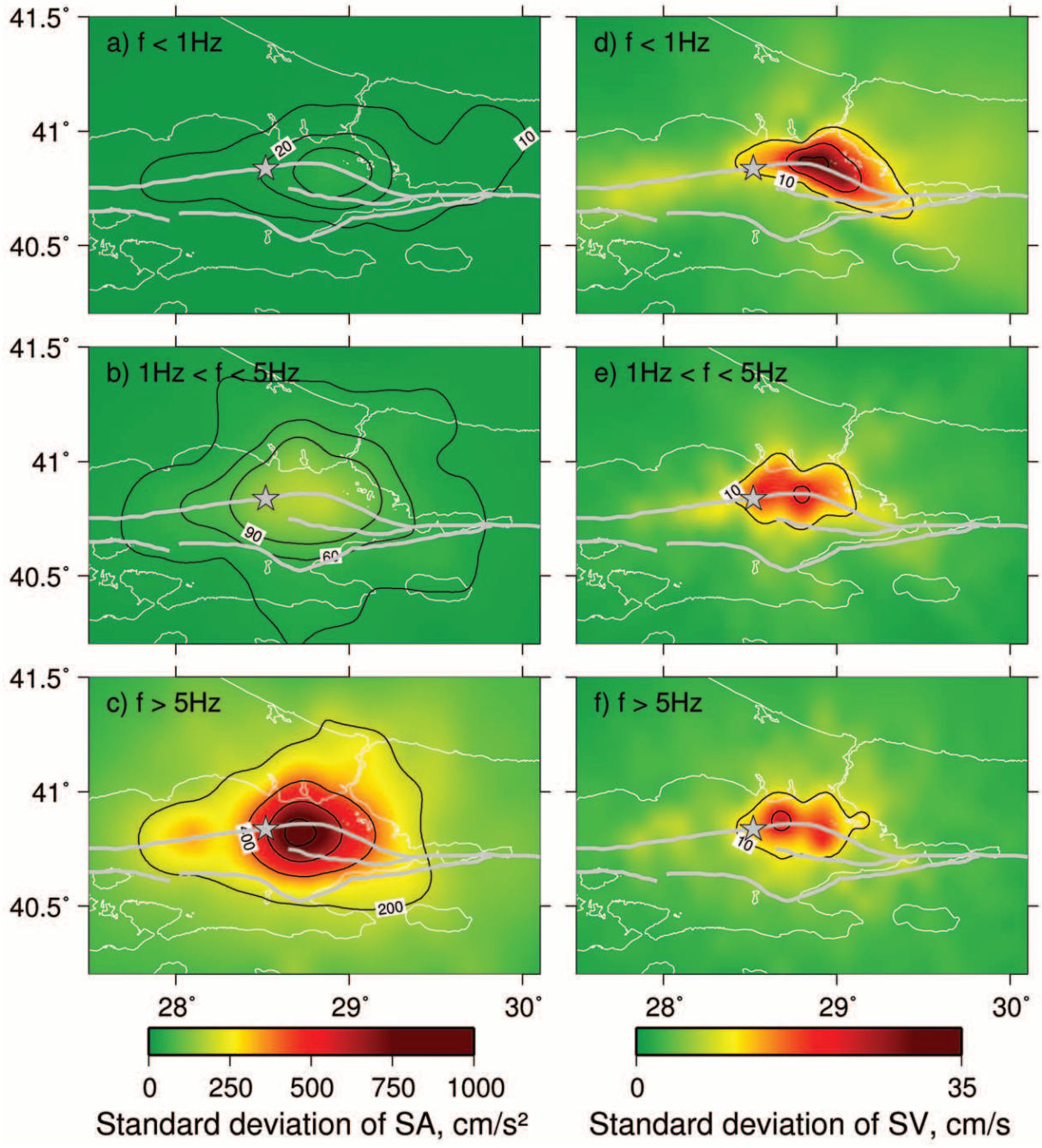

Figure 15. Distribution of standard deviation of response spectra for acceleration (a–c) and velocity (d–f). At each simulation point, the average value of the two horizontal components is used. The average response spectral values are shown in three frequency bands: (a, d) $f < 1$ Hz, (b, e) $1 < f < 5$ Hz, and (c, f) $f > 5$ Hz.

The most important parameters for the ground-motion modeling, in terms of ground-shaking levels, are the location of the rupture initiation, stress drop, rise time, rupture velocity, and the anelastic attenuation for the studied region. The impact of these parameters in frequency bands of engineering interest varies, however. From an engineering perspective, the most important parameters are the stress drop and the location of rupture initiation. Also rupture velocity and rise time will play an important role because of their strong effect on PGV. Unfortunately, these parameters are difficult to predict for future earthquakes, but detailed studies should be made ahead of ground-motion modeling, and in case of large uncertainties, extreme values should be considered in the input to the models to set bounds on the predicted ground motions.

The presented ground motions are all calculated at bed-

Table 3
Average Standard Deviation and Coefficient of Variance Based on All Simulation Sites for the Discussed Ground-Motion Measures*

Ground Motion	Average Standard Deviation	CV
PGA	75.84	0.32
PGV	11.91	0.35
SA, 0.1–1 Hz	9.03	0.18
SA, 1–5 Hz	44.10	0.22
SA, 5–10 Hz	198.67	0.29
SV, 0.1–1 Hz	5.13	0.14
SV, 1–5 Hz	3.66	0.23
SV, 5–10 Hz	4.26	0.29

*CV, coefficient of variance (standard deviation normalized by the mean); SA, spectral acceleration; SV, spectral velocity.

rock level and therefore do not take local site effects into account. When assessing the damage potential of a scenario earthquake at a given location, the local geology must be taken into consideration because the presence of soft sediments, for example, can both amplify the peak ground motions and shift the dominant frequencies of ground shaking. In this respect, the damage potential of the scenarios as discussed previously may be significantly modified by the inclusion of local site effects. At the predicted high ground-shaking levels, there is a chance that nonlinear effects may become significant, posing further challenges in the estimation of site response. This also should be kept in mind when using ground-motion simulation results for estimating seismic hazard.

In the present study, we have used one of many methodologies for estimating ground motions due to a future large earthquake. We have tested the effect of changing the various input parameters but have not discussed the issue of variation among different ground-motion-modeling methodologies. There are ongoing efforts to this end, and the discussion about these is outside the scope of this article.

Conclusions

Based on our analysis of the effect of input parameters on ground-motion simulation results we can draw the following conclusions:

- The expected effect of a M 7.5 earthquake in the Marmara Sea on the city of Istanbul will be significant with the largest ground motions occurring in the southern and southeastern parts of the city. Here, ground accelerations at the level of 500 cm/sec^2 and velocities above 50 cm/sec can be expected at bedrock level.
- Rise time, rupture velocity, rupture initiation point, and stress drop are the most significant parameters in terms of variations in ground-shaking levels. However, these parameters have their effect in different frequency bands and their engineering significance therefore varies.
- High-frequency ground motion is mainly controlled by the stress drop and Q. These parameters have a strong effect on PGA and PGA attenuation.
- Rupture velocity and rise time have a strong effect on the PGV values controlled by the coherent low-frequency ground motion.
- For the selected sites in Istanbul, the response spectra consistently show peaks at about 2 Hz and at longer periods (4 sec). The combined effect of large PGA values at high frequencies and large PGV values at longer periods could have a strong effect on the damage potential of ground motion for a wide range of buildings in Istanbul.
- The largest variability of ground motion is observed in regions adjacent to asperities as well as in the direction of rupture propagation. For PGV values the variability rapidly decreases with increasing distance to the fault. For PGA values the variability is distributed over a much wider region. The average standard deviations of all ground-motion measures are less than 35% of the mean.
- The variability of acceleration response spectra is strongly frequency dependent with a significant variation in the high-frequency part of the spectra. This reflects the dominance of high frequencies in ground-motion accelerations.
- Even though the level, distribution, and spectral values of the ground motions differ significantly, the velocity response spectra are consistent, revealing the strength of ground-motion modeling in estimating a realistic hazard for Istanbul and, hence, in risk mitigation efforts despite the large uncertainties involved. The average standard deviations of spectral amplitudes for all frequencies are only a 23% of the mean.

Our future efforts should focus on improving our ability to accurately estimate the most critical parameters influencing the ground motion, namely the rise time, rupture velocity, rupture initiation point, the stress drop, and the potential asperity locations for future earthquakes.

Acknowledgments

The present work was carried out as part of the EC project RELIEF (EVG1-CT-2002-00069). We are grateful to Yasin Fahjan who provided the codes for calculating and plotting response spectra. We also wish to thank two anonymous reviewers for providing valuable comments and suggestions for the manuscript.

References

Ambraseys, N. N., and J. A. Jackson (2000). Seismicity of the Sea of Marmara (Turkey) since 1500, *Geophys. J. Int.* **141,** F1–F6.

Atakan, K., A. Ojeda, M. Meghraoui, A. A. Barka, M. Erdik, and A. Bodare (2002). Seismic hazard in Istanbul following the 17 August 1999 Izmit and 12 November 1999 Düzce earthquakes, *Bull. Seism. Soc. Am.* **92,** 466–482.

Aydinoglu, M. N. (1998). Specification for structures to be built in disaster areas, Part III: Earthquake disaster prevention, Ministry of Public Works and Settlement, Government of Republic of Turkey, Official Gazette, no. 23390.

Barka, A., H. S. Akyüz, E. Altunel, G. Sunal, Z. Cakir, A. Dikbas, B. Yerli, R. Armijo, B. Meyer, J. B. de Chabalier, T. Rockwell, J. R. Dolan,

R. Hartleb, T. Dawson, S. Christofferson, A. Tucker, T. Fumal, R. Langridge, H. Stenner, W. Lettis, J. Bachhuber, and W. Page (2002). The surface rupture and slip distribution of the 17 August 1999 Izmit earthquake (M 7.4), North Anatolian fault, *Bull. Seism. Soc. Am.* **92,** no. 1, 43–60.

Birgören, G., O. Özel, Y. Fahjan, and M. Erdik (2004). Determination of site effects in Istanbul area using a small earthquake record of the dense strong motion network, presented at XXIX General Assembly of the European Seismological Commission, Potsdam, Germany, poster no. 249.

Bouchon, M. (1981). A simple method to calculate Green's functions for elastic layered media, *Bull. Seism. Soc. Am.* **71,** 959–971.

Bouchon, M., M.-P. Bouin, H. Karabulut, M. N. Toksos, M. Dietrich, and A. J. Rosakis (2001). How fast is rupture during an earthquake? New insights from the 1999 Turkey earthquakes, *Geophys. Res. Lett.* **28,** no. 14, 2723–2726.

Dalguer, L. A., H. Miyake, and K. Irikura (2004). Characterization of dynamic asperity source models for simulating strong ground motion, presented at Proceedings of the 13th World Conference on Earthquake Engineering (WCEE), Vancouver, Canada, August 2004, paper no. 3286.

Das, S., and B. V. Kostrov (1986). Fracture of a single asperity on a finite fault: a model for weak earthquakes? In *Earthquake Source Mechanism*, S. Das, J. Boatwright, and C. Scholz (Editors), American Geophysical Union, Washington, D.C., 91–96.

Erdik, M., M. Demircioglu, K. Sesetyan, E. Durukal, and B. Siyahi (2004). Earthquake hazard in Marmara Region, Turkey, *Soil Dyn. Earthquake Eng.* **24,** 605–631.

Gurbuz, C., M. Aktar, H. Eyidogan, A. Cisternas, H. Haessler, A. Barka, M. Ergin, N. Turkelli, O. Polat, S. B. Ucer, S. Kuleli, S. Baris, B. Kaypak, T. Bekler, E. Zor, F. Bicmen, and A. Yoruk (2000). The seismotectonics of the Marmara region (Turkey): results from a microseismic experiment, *Tectonophysics* **316,** 1–17.

Harris, R. A., J. F. Dolan, R. Hartleb, and S. M. Day (2002). The 1999 Izmit, Turkey, earthquake: a 3D dynamic stress transfer model of intraearthquake triggering, *Bull. Seism. Soc. Am.* **92,** no. 1, 245–255.

Hubert-Ferrari, A., A. Barka, E. Jacques, S. S. Nalbant, B. Meyer, R. Armijo, P. Tapponnier, and G.C.P. King (2000). Seismic hazard in the Marmara Sea region following the 17 August 1999 Izmit earthquake, *Nature* **404,** 269–273.

Irikura, K. (1986). Prediction of strong acceleration motion using empirical Green's function, in *Proc. of the 7th Japan. Earthquake Eng. Symp.*, 151–156.

Oglesby, D. D., P. M. Mai, K. Atakan, D. Pantosti, and S. Pucci (2005). Dynamic rupture in the presence of fault discontinuities: an application to faults in the Marmara Sea, Turkey (abstract), AGU Fall Meeting, San Francisco, 5–9 December, S33C-03.

Okay, A. I., A. Kaslilar-Özcan, C. Imren, A. Boztepe-Güney, E. Demirbag, and I. Kuscu (2000). Active faults and evolving strike-slip basins in the Marmara Sea, northwest Turkey: a multichannel seismic reflection study, *Tectonophysics* **321,** 189–218.

Parsons, T. (2004). Recalculated probability of $M \geq 7$ earthquakes beneath the Sea of Marmara, Turkey, *J. Geophys. Res.* **109,** B05304, doi 10.1029/2003JB002667.

Parsons, T., S. Toda, R. S. Stein, A. Barka, and J. H. Dietrics (2000). Heightened odds of large earthquakes near Istanbul: an interaction-based probability calculation, *Science* **288,** 661–665.

Pulido, N., and T. Kubo (2004). Near-fault strong motion complexity of the 2000 Tottori earthquake (Japan) from a broadband source asperity model, *Tectonophysics* **390,** 177–192.

Pulido, N., A. Ojeda, K. Atakan, and T. Kubo (2004). Strong ground motion estimation in the Sea of Marmara region (Turkey) based on a scenario earthquake, *Tectonophysics* **391,** 357–374.

Somerville, P., K. Irikura, R. Graves, S. Sawada, D. Wald, N. Abrahamson, Y. Iwasaki, T. Kagawa, N. Smith, and A. Kowada (1999). Characterizing crustal earthquake slip models for the prediction of strong ground motion, *Seism. Res. Lett.* **70,** 59–80.

Sørensen, M. B., K. Atakan, and N. Pulido (2007). Simulated strong ground motions for the great M 9.3 Sumatra-Andaman earthquake of 26 December 2004, *Bull. Seism. Soc. Am.* **97,** no. 1, S139–S151, doi 10.1785/0120050608.

Sørensen, M. B., I. Oprsal, S. Bonnefoy-Claudet, K. Atakan, P. M. Mai, N. Pulido, and C. Yalciner (2006). Local site effects in Ataköy, Istanbul, Turkey, due to a future large earthquake in the Marmara Sea, *Geophys. J. Int.* **167,** 1413–1424, doi 10.1111/j.1365-246X.2006.03204.x.

Straub, C., H.-G. Kahle, and C. Schindler (1997). GPS and geologic estimates of the tectonic activity in the Marmara region, NW Anatolia, *J. Geophys. Res.* **102,** 27,587–27,601.

Tezcan, S. S., E. Kaya, I. E. Bal, and Z. Özdemir (2002). Seismic amplification at Avcilar, Istanbul, *Eng. Struct.* **24,** 661–667.

Department of Earth Science
University of Bergen
Allegt. 41
5007 Bergen, Norway
(M.B.S., K.A.)

National Strong Motion Mapping Project
National Research Institute for Earth Science
and Disaster Prevention (NIED)
3-1, Tennodai, Tsukuba
Ibaraki, 305-0006, Japan
(N.P.)

Manuscript received 24 February 2006.